A loading model for an OWC caisson based upon large-scale measurements

A Loading Model for an OWC Caisson based upon large-scale Measurements

Krisna A. Pawitan[a], Aggelos S. Dimakopoulos[b], Diego Vicinanza[c], William Allsop[d], Tom Bruce[a]

a *School of Engineering, The University of Edinburgh, King's Buildings, Edinburgh EH9 3JL, United Kingdom*
b *HR Wallingford, Howbery Park, Wallingford OX10 8BA, United Kingdom*
c *Department of Engineering, University of Campania "Luigi Vanvitelli", via Roma 9, 81031 Aversa (CE), Italy.*
d *William Allsop Consulting Ltd., The White House Denchworth Road, Grove, Wantage, Oxon, England, OX12 0AR, United Kingdom*

Abstract

Wave energy is one of the most promising marine energy resources in terms of the scale of the resource, but there remains little technology convergence and costs remain at near-prohibitive levels. Of many wave energy converter (WEC) concepts that have been developed over the years, the oscillating water column (OWC) stands out for its simplicity and low maintenance cost. Quite some experience of actual OWC operation has been gained to date from small, stand-alone pilot schemes. One way to reduce costs is the integration of an OWC-WEC into a breakwater, enabling some degree of cost-sharing between energy and harbour or coastal defence functions. A major problem encountered during the design of an OWC-WEC scheme remains the uncertainty in the wave loads, with their critical influence upon capital cost. A model to estimate forces acting on an OWC chamber in a caisson breakwater is proposed in this paper. Horizontal forces on the front (curtain) wall and the rear (in-chamber) wall are predicted. In addition, and unlike a conventional caisson breakwater, vertical forces acting on the caisson chamber ceiling will have considerable effect on sliding and overturning characteristics of the breakwater structure. The proposed model enables the prediction of chamber pressures which in turn influence the chamber vertical force. The new model has been compared with results from large scale physical model measurements from tests carried out in the very large wave channel, GWK, in Hannover (Germany). Forces under both regular and irregular wave conditions were measured. The comparisons show that the model fits well with the test results to the factor of 1 ± 0.2 for the regular wave cases and to the factor of 0.8 ± 0.2 for irregular wave cases. This model will enable the structural design of caisson breakwater-integrated OWCs to be approached with uncertainties reduced to those comparable with conventional caisson design.

1. Introduction

Over the last 70 years, wave energy has been identified as offering one of the largest resources of marine renewable energy (Falcão & Henriques, 2015). The United Kingdom has played a leading role in development to date. Full scale devices have been deployed, such as LIMPET in 2000 (*e.g.* Boake *et al*.,2002), Pelamis in 2004 (*e.g*. Retzler, 2006) and Oyster in 2012 (*e.g.* Folley *et al*., 2004). Despite successes, WECs have not reached large-scale deployment due to stubbornly high construction costs (Azzellino *et al*., 2011). These are partly due to the sheer size of the device and the aggressive locations for deployment. One way to reduce costs is the integration of an OWC-WEC into a breakwater, enabling some

degree of cost-sharing between energy and harbour / coastal defence functions. A shore-connected OWC breakwater will also help access for maintenance.

Over the years, two types of WEC-installed breakwaters have been explored: caisson OWCs *e.g.* Arena *et al*. (2013); Boake *et al*. (2002); Boccotti (2003); Neumann & Crom (2011); Patterson *et al*. (2009); Raju & Neelamani (1992); Takahashi (1988); Takahashi *et al*. (1992); Torre-Enciso *et al*. (2010) and wave overtopping devices mounted on seawalls and rubble mound breakwaters, *e.g.* Buccino *et al*. (2012); Buccino *et al*. (2015a); Buccino *et al*. (2015b); Buccino *et al.* (2016); Contestabile *et al*. (2017); Iuppa *et al*. (2016); Vicinanza *et al.* (2015); Vicinanza *et al*. (2013); and Vicinanza *et al*. (2014). The device types differ in fundamental energy harvesting principle. OWC devices use the incident wave to induce an up and down motion of the water column inside the caisson to pump air in and out through the power take-off mechanism. The wave overtopping devices, on the other hand, use a slope with a reservoir behind the crest to capture overtopping flows, from which water then recirculates back to the sea through the power take-off mechanism. Conventionally, both methods use a turbine as power take-off, though recent development suggest a possibility of using an electroactive membrane for an OWC type device (Moretti *et al*., 2015).

It is important for a designer of an OWC caisson to be able to estimate extreme loads to design against sliding and/or overturning of the structure. The importance of assessing loads reliably is strengthened by the need for reliability and operability, given that they are exposed to the open sea. An example where these difficulties were manifest was the OWC breakwater at the port of Mutriku, in the Basque region of Spain. The scheme, operational since 2012, is a 16-chamber OWC rated at 300 kW. During its construction, however, it suffered major damage during storms in 2007, 2008, and most seriously of all, in 2009 (Medina-Lopez *et al*., 2015).

This incident highlights the needs for better research on loadings of the whole structure. This paper derives a conceptual model to estimate pressure distributions over an OWC caisson.

An early attempt of in-chamber rear wall force estimation was postulated by Patterson*, et al.* (2009) but was not accompanied by supporting experiment. Physical model studies to determine the pressure acting on the rear wall of OWC caisson have been done using small-scale experiment of 1:40 and 1:60 (Kuo *et al*., 2015), while the influence of air damping characteristic on the front wall force has also been explored using a small-scale experiment of 1:81 (Pawitan & Bruce, 2016). Morris-Thomas *et al.* (2007) further explored the influenced of the front wall geometry to the over-all hydrodynamic efficiency and concluded that it has minimal influence with peak efficiency achieved during the experiment equal to 0.7. Recent exploration of forces and pressures acting on a breakwater installed OWC typed WEC found that shoreward pressures dominated other load directions acting on the structure (Ashlin *et al.,* 2017). Those experiments also found that the horizontal force may be twice the vertical force experienced by the structure. The experiment however only used regular wave conditions,. Furthermore, their conclusions were drawn only for a closed chamber, not representative of the OWC during operation.

This work reported in this paper seeks to deliver a loading prediction model for this class of structure. To do this in general, the model will need to examine, under irregular wave conditions, not only front face loadings (which may be similar to, or differ from, those on a conventional vertical caisson), but also the load experience within the OWC chamber; on the

rear wall and also potentially on the chamber's ceiling. Later, the validity and accuracy of the conceptual model is checked using measurements from a large-scale physical model study.

The model proposed in this paper will be explained in Section 2. The experimental set-up to validate the model from the large-scale measurements will be described in Section 3. Comparison of results with the conceptual model will be shown in Section 4 along with the analysis of the results and discussion on irregular waves effect. Section 5 will discuss the uncertainties of wave loadings, scaling effect of the air characteristics, model testing limitations, and the conceptual model evaluation. Conclusion will be drawn in Section 6.

2. Conceptual model

2.1. Motivation for conceptual model

These sections explore the rationale for developing a conceptual loading model, the introduction and justification of the concepts and equations used, and the classification of the chamber conditions to which the model can be applied.

There are a wide and trusted literature that discuss the pressure distribution for design of a vertical breakwater against sliding or overturning due to wave loads. A prediction tool for the loadings experienced by an OWC caisson must in addition contain a prediction tool to give practical and conservative estimates of the pressure distributions which occur inside the chamber: on the rear wall; on the ceiling, and on the inside of the front curtain wall. Only with all of these can the whole structure be designed for stability and robustness. This paper aims to provide a conceptual model to predict the pressure distribution on the real wall and the caisson ceiling. For this model, the water column is assumed to be well behaved without sloshing, and the water level inside the chamber is assumed never to reach the opening 'lip' of the front wall, *i.e.* no 'venting' occurs. Wave pressures acting on the inside of the front (curtain) wall will have an opposite direction to pressures acting on the rear wall, so it is safe to assume that calculating this pressure can only increase the stability of the overall structure. This allows the conceptual model to add a degree of safety by removing the pressure estimation acting on the inside of the curtain wall from the equation for force per metre run.

The conceptual model for in-chamber pressure estimation is described in the following sub-sections. For navigation, see Figure 1.

2.2. Proposed model equation and definition

Goda (2000) presents an estimation method for design wave loads for a vertical breakwater. The concept proposed in this section adoptes the Goda pressure estimation method as the starting point. Imagine F_{Goda} as the force estimation acting on the front wall of a conventional breakwater calculated using the Goda method. It is then hypothesised that the pressure 'reaching' the rear wall of the OWC chamber results from that proportion of the wave momentum transmitted past the front curtain wall of the structure. This hypothesised situation is similar to that of a skirt breakwater, so a method to calculate the transmission coefficient (K_t) is adopted from the skirt breakwater situation. Kriebel & Bollman (1996) developed a method which estimates K_t based on Equations 1 and 2,

$$0 \leq \frac{w}{d} \leq 0.3 \rightarrow \quad K_t = 1 \qquad (1)$$

$$0.3 < \frac{w}{d} \leq 0.9 \quad \rightarrow \quad K_t = \frac{0.81 - 0.7(^{w}/_{d})}{0.6} \qquad (2)$$

where d is the water depth above the floor of the chamber and the submergence depth of the front wall (skirt) into the water (w), Figure 2.

The simplification of K_t calculation is adopted in this conceptual method and can be seen in Equation 1 and 2 with w/d defined as the wall penetration factor. Values of wall penetration factor are only considered up to 0.9, because it is assumed that at higher factor, no wave momentum will be able to pass through the wall opening. On the contrary, for wall penetration factors less than 0.3, the front wall is considered to have negligible reduction of transmitted wave momentum.

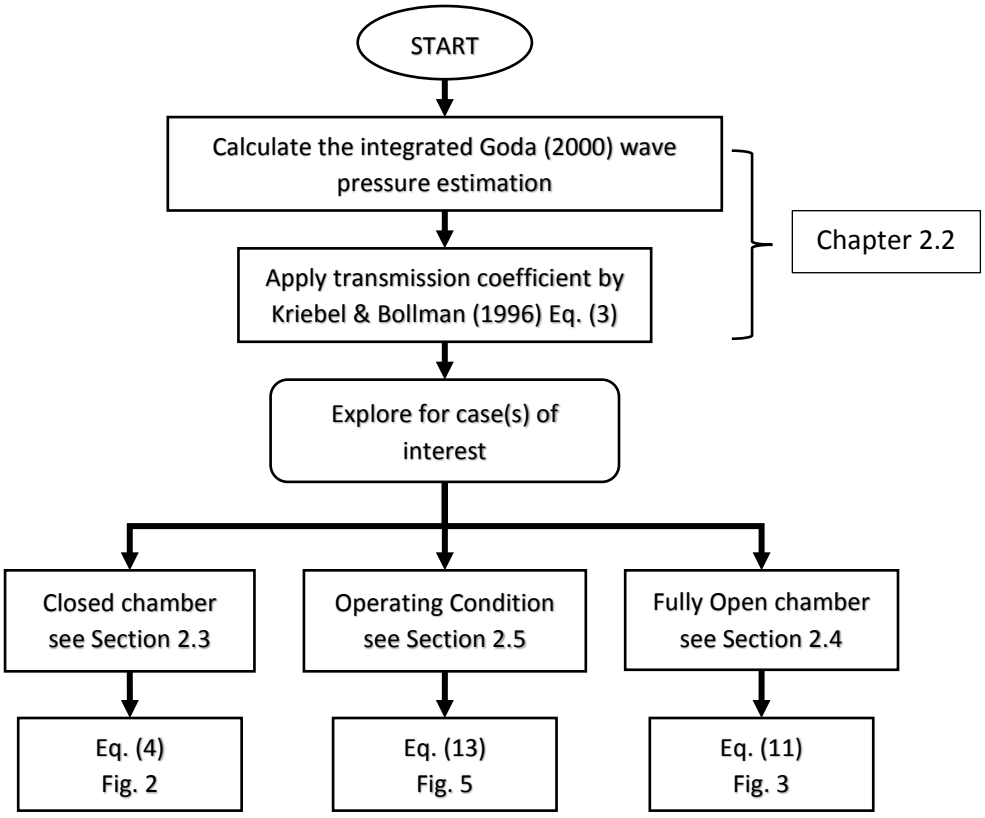

Figure 1 The flowchart of proposed model calculation process

If F_{rw} is taken as the transmitted force which passes through the front wall, then the relationship between F_{Goda} and F_{rw} can be expressed using Equation 3.

$$F_{rw} = F_{Goda}.K_t \qquad (3)$$

Since Equation 3 only estimates the force acting on the rear wall of the OWC chamber, next step is to determine the pressure distribution acting on the rear wall of the OWC chamber, which is expected to vary significantly depending on the power take-off (PTO) resistance. The PTO resistance however, may be imagined to lie between two extreme conditions: that of a closed OWC chamber (100% PTO resistance, zero air flow in or out of chamber) and a fully open chamber (0% PTO resistance, free flow of air in chamber). Before exploring a model for the 'operating' regime between these extremes, it will be instructive to explore

these extremes first, in Sections 2.3 and 2.4, for closed and fully open chamber respectively. The operating condition is then explored in Section 2.5.

2.3. Closed chamber condition

The fully closed chamber means there is no air movement into or out of the chamber, with the consequence that water movement into or out of the chamber is minimal, depending on the air compressibility characteristics inside the chamber. As a result, it can be anticipated that this closed condition will result in the highest chamber pressures. Whilst air is inherently compressible, the hydraulic forces in small-scale tests are very small in absolute terms so the air in the (model) OWC chamber will be very stiff relative to the (model) wave forces. In effect, small scale air can be treated as incompressible (Weber, 2007, Dimakopoulos *et al.* 2017). The motion of water level within the chamber is minimal and can therefore be assumed to be stationary. Because the in-chamber water is not moving into or out of the chamber, pressure variations due to velocity and cyclical / rotational motions that would create a non-uniform distribution are not expected to occur. Hence the wave pressure will transmit as an increment to the hydrostatic pressure at still water level and will be uniform in both air and water phases, giving a rectangular pressure distribution for the transmitted force (F_{rw}) acting on the rear wall as shown in Figure 2.

Here F_{Goda} denotes the front wall force explained in the previous sub-section. Since the chamber pressure (relative to atmosphere) is driven by the dynamic water pressure, the chamber pressure will therefore be the same as the water pressure. The water pressure inside the chamber denoted by p_c can be calculated using Equation 4 with d as the water depth in the OWC chamber.

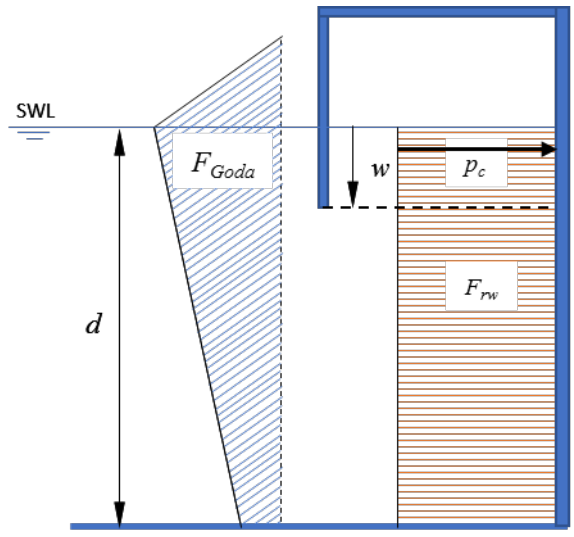

Figure 2 The pressure distribution schematics for the closed chamber case

$$(F_{rw})_{closed} = K_t . F_{Goda} = p_c d \qquad (4)$$

2.4. Open chamber condition

The other extreme is the situation of the fully open chamber. In this case, air damping in the chamber will be zero and pressures inside the chamber will remain very close to atmospheric. This condition, then, allows the water inside the chamber to move freely up and down depending on the wave height transmitted under the front wall (skirt). In the idealised view, chamber water motion will only be driven by the wave transmitted into the caisson without any resistance. The pressure distribution inside the chamber is therefore postulated to be similar to the pressure distribution on the front wall. This pressure distribution on the rear wall for the fully open case is shown in Figure 3, annotated with the parameters used for the estimation method that follows.

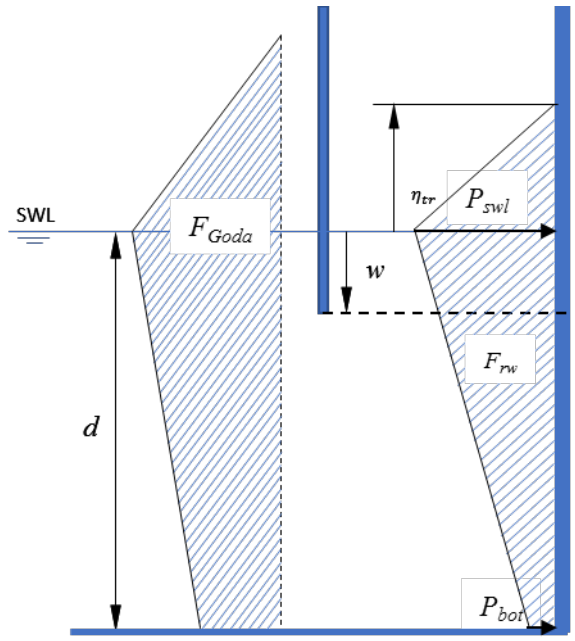

Figure 3 The pressure distribution schematics for the fully open chamber case

The postulated pressure distribution is similar to the Goda distribution and the calculation is thus adopted directly from that calculation as applied to a plain vertical breakwater. In this model, H_{tr} denotes the transmitted wave height as given by Equation 5.

$$H_{tr} = H_{max}\, K_t \qquad (5)$$

Following Goda, coefficients α_{swl} and α_{bot} are introduced in Equations 6 and 7,

$$\alpha_{swl} = \left[0.6 + 0.5\left(\frac{4\pi h/L}{\sinh(4\pi h/L)}\right)^2\right] + \left[\min\left\{\frac{h_b - d}{3h_b}\left(\frac{H_{tr}}{d}\right)^2, \frac{2d}{H_{tr}}\right\}\right] \qquad (6)$$

$$\alpha_{bot} = 1 - \frac{d}{h}\left[1 - \frac{1}{\cosh(2\pi h/L)}\right] \qquad (7)$$

where h is the full water depth of the incoming wave in front of the structure, L denotes the deep-water wave length, and h_b denotes the depth at 5H seaward of the structure. These dimensions are then used to estimate the pressure at the still water level (P_{swl}) and at the bottom of the rear wall (P_{bot}) – Equations 8 and 9 respectively.

$$P_{swl} = \alpha_{swl}\, \rho\, g\, H_{tr} \qquad (8)$$

$$P_{bot} = \alpha_{bot}\, P_{swl} \qquad (9)$$

The elevation to which the transmitted wave height (H_{tr}) acts is denoted by η_{tr} and calculated using Equation 10,

$$\eta_{tr} = 1.5\, H_{tr} \qquad (10)$$

Equations 8, 9 and 10 can then be substituted into Equation 3 to give the total force on the rear wall of the chamber (Equation 11).

$$(F_{rw})_{open} = 0.5\big((\eta_{tr} + d)P_{swl} + dP_{bot}\big) \qquad (11)$$

2.5. Operating condition

As mentioned earlier, the "operating condition" is the condition where a power take-off resists motion of the water column to some degree. Because this condition lies between the extremes of the closed and open chamber, the pressure distribution is postulated to be an intermediate condition between the two. If the proportion (or weighting) of the closed chamber situation in the whole transmitted force (F_{rw}) is denoted by P (with $0 \leq P \leq 1$), then the F_{rw} force can be given by Equation 12.

$$(F_{rw})_{operate} = P(F_{rw})_{closed} + (1 - P)(F_{rw})_{open} \qquad (12)$$

This equation combines the extreme conditions with the first term on the right-hand side representing the weighted contribution of the closed chamber pressure distribution and the second term representing the contribution due to an open chamber pressure distribution. The assumption of a static chamber water surface used in Equation 4 for the closed chamber case is no longer applicable in the operating case, so an elevation η_{tr} needs to be added for the closed chamber equation. This adjustment makes the full operating pressure distribution equation (Equation 13):

$$(F_{rw})_{operate} = P\big(p_c(d + \eta_{tr})\big) + 0.5(1 - P)\big((\eta_{tr} + d)P_{swl} + dP_{bot}\big) \qquad (13)$$

with the newly adjusted η_{tr} for this condition given in Equation 14,

$$\eta_{tr} = \begin{cases} 0, \ if\ P = 1 \\ \min(1.5\, H_{tr}\, , h_{ceil}), \ if\ 0 \leq P < 1 \end{cases} \qquad (14)$$

where h_{ceil} denotes the height of the chamber ceiling (above swl), since the wave height will not be able to exceed the chamber ceiling. The weighting coefficient (P) varies depending on the air damping characteristic of the OWC chamber, which ultimately related to the PTO resistance. A highly simplified relation between P and the air damping characteristic is shown in Figure 4.

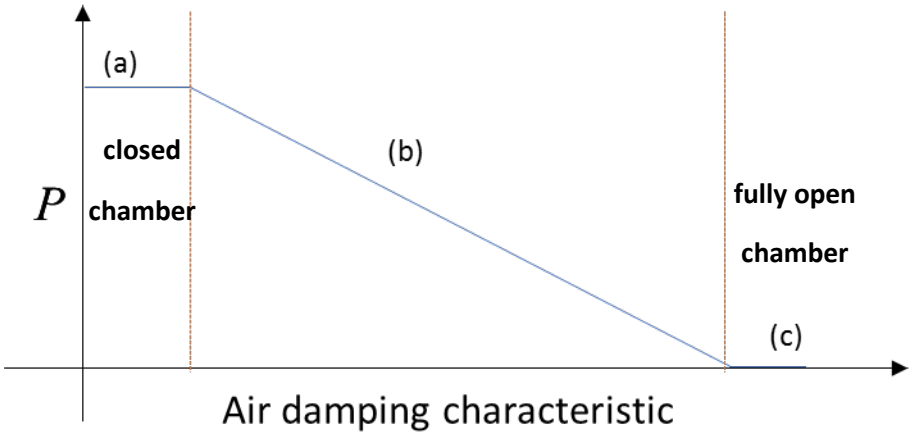

Figure 4 The P coefficient expected relation with the air damping characteristics divided into three regimes: (a) the air damping reduction is small enough to be neglected with P = 1, (b) the air damping reduced toward zero leading to the chamber pressure dropped considerably with P = f(Air damping), and (c) the air damping is small enough to be considered as fully open with P = 0

Recalling that $P = 1$ means the chamber can be considered closed and P = 0 means the chamber can be considered fully open, Figure 5 (a) – (e) show the schematic diagrams postulated for the pressure distributions on the rear wall of an OWC chamber formed in a vertical breakwater, for P = 1, 0.75, 0.5, 0.25, and 0 respectively. The diagrams are schematics only but are intended to show the way in which the pressure distribution adjusts from closed chamber to fully open via a smooth transition through the 'operating' regime.

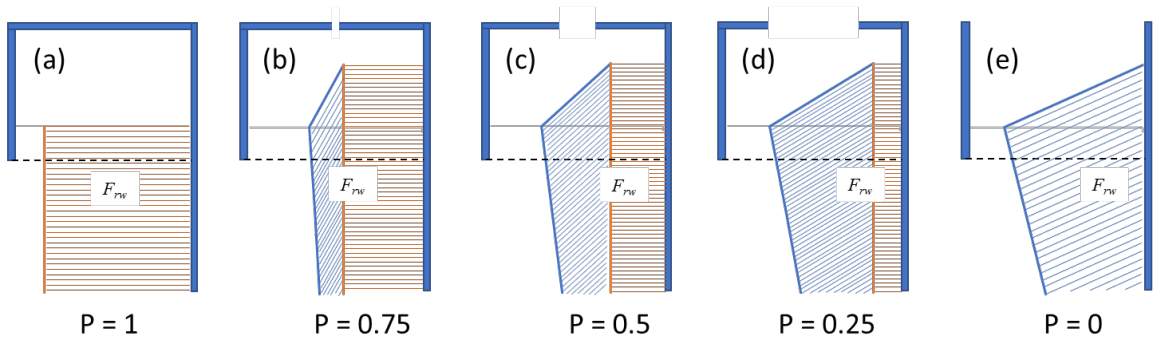

Figure 5 The pressure distribution schematics for the operating condition case at various proportion coefficient P values. Opening sizes exaggerated for illustrative purpose. P=1, subfigure (a) illustrate closed chamber, P=0 (e) illustrate fully open chamber, and subfigures (b), (c), and (d) illustrate intermediate cases identified as 'operating cases'

3. Experimental setup

To validate the model proposed, data have been used from large scale experiments carried out in the large wave channel (Grosse Wellenkanal, GWK) in Hannover, Germany. The "GWK OWCs" project was an EC Hydralab III access project led by University of Edinburgh in collaboration with HR Wallingford, University of Campania "Luigi Vanvitelli", Naples, Queen's University of Belfast, and the University of East Anglia. The test programme is described in detail in Allsop *et al.* (2014) and Viviano *et al.* (2016).

The flume is 307 m long x 5 m wide x 7 m deep. Wave heights up to 2 m are achievable for regular waves, with $H_{m0,i}$ up to 1.3 m achievable for the irregular waves. The structure installed consisted of three caissons located approximately 100 m from the wave maker.

The OWC caisson geometry was fixed, but the still water depth (h) and orifice opening diameter (d_0) were controlled. Orifice opening diameters were selected between zero (closed chamber) to 0.3 m (approximating a fully open situation). All three chambers used the same orifice diameter.

Schematics of the experimental arrangement at GWK are shown in Figure 6 from the side view (a) and the plan view (b) along with the detailed location of the wave gauges with dimension shown in m. Eight wave gauges measured the wave conditions: four wave gauges (WG01-04) were located at the full depth zone where the bottom is flat; the other four wave gauges (WG05-08) were located 1 m in front of the structure with 1 m distance in between them. The foreshore leading to the structure has 1:6 inclination. These arrangements allow the wave reflection to be analysed using a 4 probes method – see Faraci *et al*. (2015). The wave reflection analysis results conclude that under irregular waves conditions, the 0.2m orifice diameter (0.88%) yields the least reflection and therefore optimum energy extraction (Viviano *et al*., 2016). The detailed longitudinal section of the centre caisson of the structure and the location of the pressure sensors is indicated in Figure 7. Five further wave gauges (WG09-13) are located inside the caisson chamber – one close to each corner and one in centre of the chamber – to measure the water surface elevations inside the chamber.

A line of five pressure transducers were placed vertically on the front wall facing outside (P1-5) and on rear wall facing into the chamber (P8-12). Two pressure sensors were mounted in the ceiling facing down into the chamber (P6 and P7). Figure 8 (a) and (b) show the facility, along with the three identical structures used for the experiment, before the installation of the load-bearing front wall. Figure 8 (c) shows the inside view of the caisson chamber. The lines drawn on the wall represent the distance from the ceiling. The orifice used to provide damping was mounted in a 0.5 m diameter 'chimney' above the centre of the chamber, both to avoid influence of overtopped water and to enable the orifice to serve the additional purpose of giving a further (approximate) measure of air flowrate. Figure 9 shows the complete structure with the front wall just before the experiment (a) and during the experiment (b). Although only the central chamber (of the three) was instrumented, the other two chambers were hydraulically identical, with the same orifice plates.

In the operating condition, the air damping characteristics inside the chamber will change depending on the power-take-off (PTO) resistance. To vary the damping characteristic of the PTO, five different orifice diameters were used: 0.05 m (0.06%), 0.1 m (0.22%), 0.2 m (0.88%), and 0.3 m (1.99%). In addition, a fully closed caisson chamber (orifice diameter = 0 m) was tested. The 0.3 m orifice approximates the fully open condition, offering very little resistance to the air flow. The opening diameters from 0.05 m to 0.2 m represent the operating conditions.

Both regular and irregular waves were generated at various wave steepness (s and s_p) as shown in Figure 10 (a) and (b) respectively. The detailed wave condition name, wave height,

and wave period can be seen in Table 1 for regular wave tests and Table 2 for irregular wave tests. These steepnesses are calculated based on the wave height (H) and wave period (T) for the Regular wave condition (Equation 15) and significant wave height (H_{m0}) and significant wave period (T_p) for the Irregular wave condition (Equation 16). Both (significant) wave height and wave period were measured on the deeper (horizontal) part of the flume.

$$\text{For regular waves: } s = 2\pi H / gT^2 \quad (15)$$

$$\text{For random waves } s_p = 2\pi H_{m0}/gT_p^2 \quad (16)$$

The further detailed tested wave conditions along with the reference name are listed in for the regular waves and for the irregular waves. The irregular waves were generated using JONSWAP spectrum with a peak enhancement factor (γ) of 3.3. Several wave conditions were tested more than once to ensure the repeatability of the experiment. Variation in front wall pressure maxima were found to be less than 4.5% over 4 repeats, giving good confidence in repeatability. Viviano *et al*. (2016) gives full details.

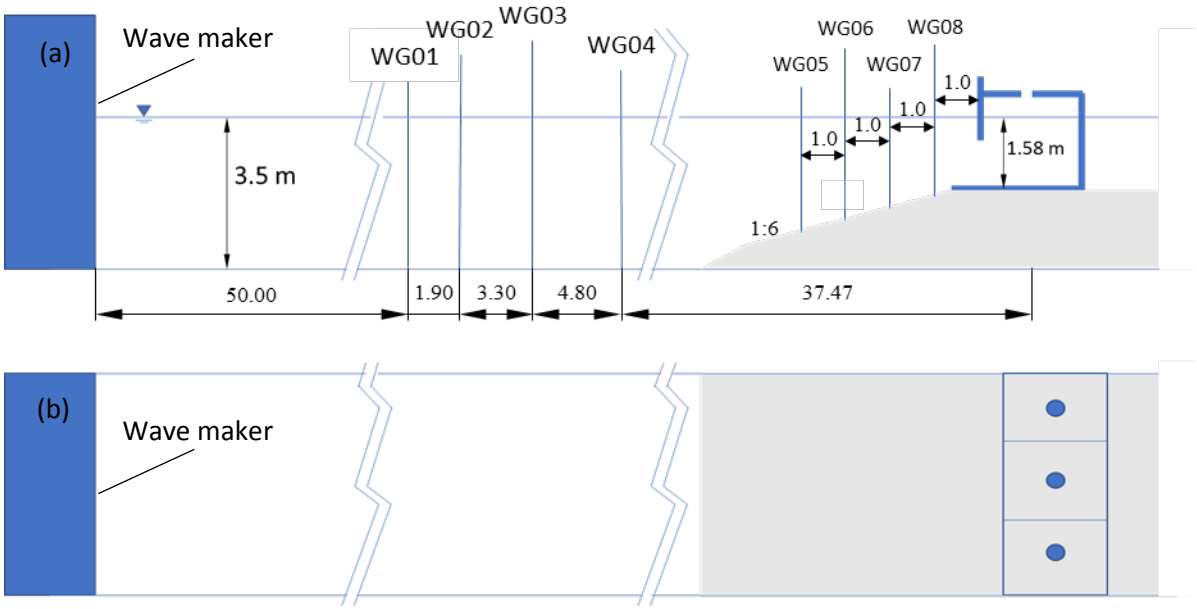

Figure 6 Experimental setup at GWK from (a) longitudinal section with the water depth for both the deeper part and the shallower part in m, and (b) top view. The waves travel from left to right with the paddle to OWC length = 97.47 m. The distance between the WG01-WG04 wave gauges and wave maker; and the WG05-WG08 wave gauges to the structure are shown in m.

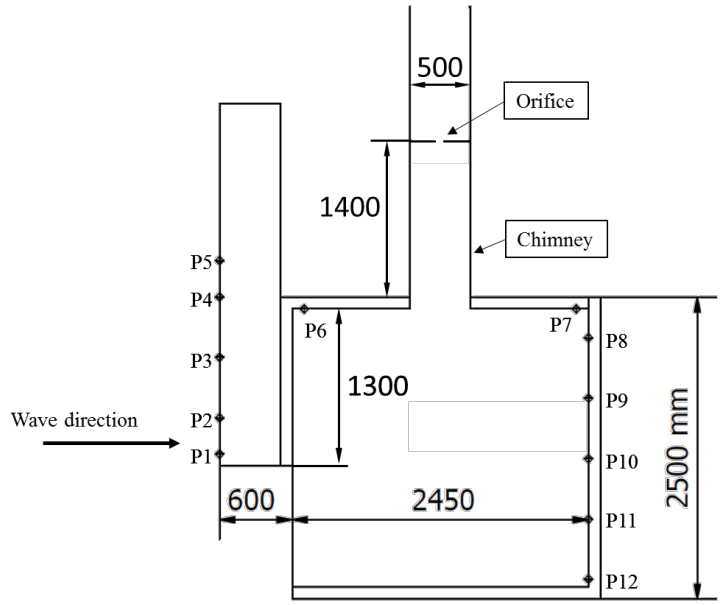

Figure 7 Detailed longitudinal section of the OWC device. P1 to P5 indicate the location of the front face pressure transducers; P6 and P7 for the chamber ceiling pressures, and P8 to P12 for the pressures on the rear wall of the chamber. All the dimensions are in mm.

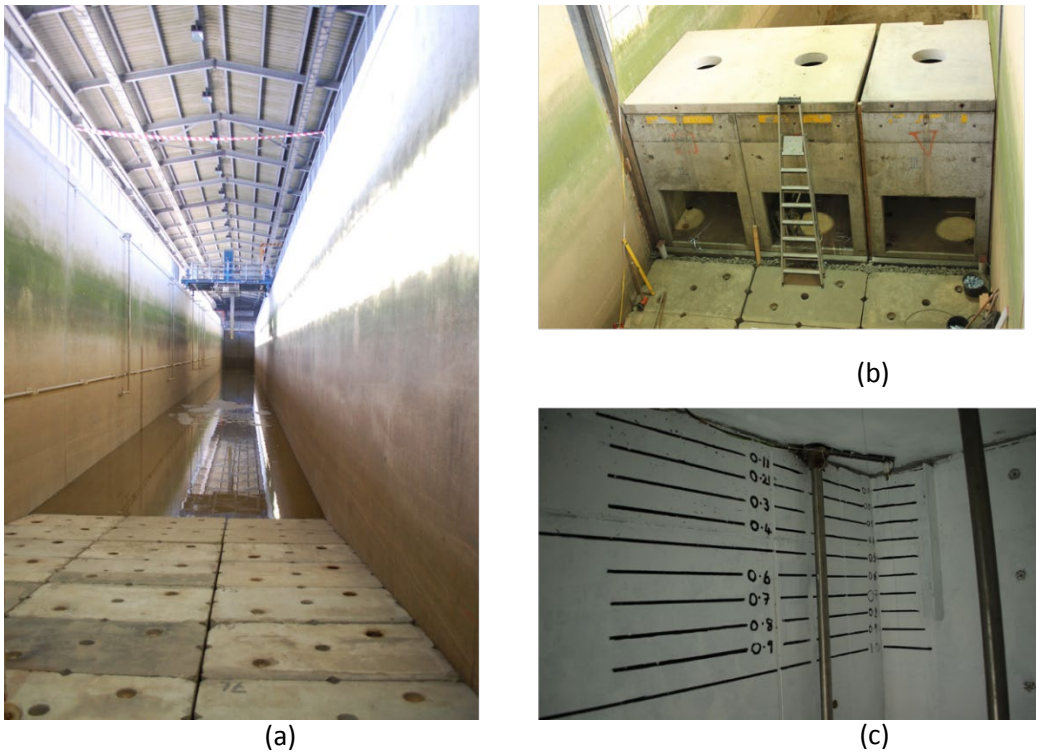

Figure 8 Photographs of (a) the empty GWK flume, (b) three OWC caissons tested, and (c) Insider view of the caisson chamber.

(a) (b)

Figure 9 The complete OWC structure (a) before the experiment and (b) during the experiment

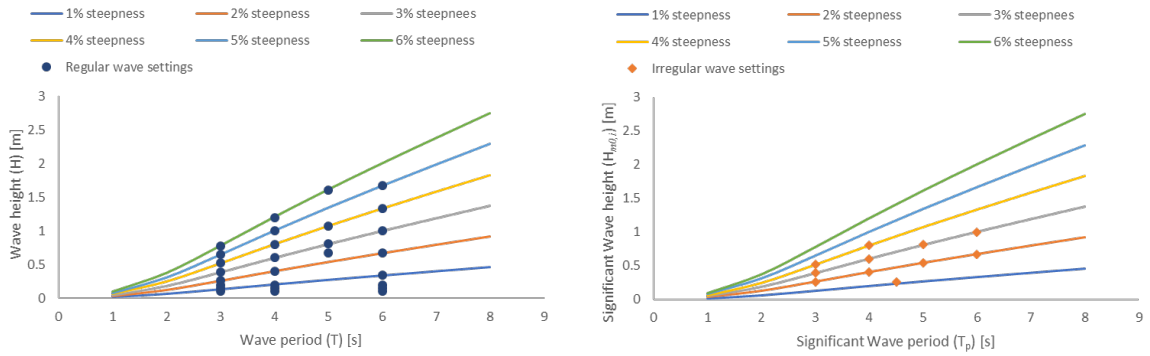

(a) (b)

Figure 10 Wave conditions used for the experiments at selected wave steepnesses for (a) regular waves, and (b) irregular waves.

Since the model is validated with a large-scale physical model, is it important to understand the scaling method used for the model. Arguably, the most important scaling considerations in designing a physical model experiment of a breakwater installed OWC are the hydraulic ratio of gravity and inertial forces and the caisson chamber's air elasticity. The Froude number (N_{Fr}, Equation 17) expresses the relative influence of inertial and gravity forces which is universally used in hydraulic physical modelling to keep the gravity:intertial force ratio correct.

$$N_{Fr} = \frac{V}{\sqrt{g\,L}} \qquad (17)$$

Here V, g and L are velocity, acceleration due to gravity and the characteristic length scale respectively. Cauchy number (N_{Ca}, Equation 18) is a ratio of the inertial to the elastic forces which is often used to maintain the influence of fluid compressibility.

$$N_{Ca} = \frac{\rho V^2}{E} \quad (18)$$

In this equation, V, ρ and E are the velocity, fluid density and fluid elasticity respectively.

The hydraulic similitude of a breakwater installed OWC model can, in principle, be ensured by keeping both numbers the same between the model and the prototype, $(N)_p = (N)_m$. Unfortunately, keeping Froude number the same will result in different Cauchy number and *vice versa*. For the sake of model simplicity, only Froude scaling is considered in this large-scale experiment. This forces an assumption that effects die to the air's compressibility are the same in the model as at prototype scale. An extensive study regarding the air elasticity effect has been done both using experimental approached (see Weber, 2007) and computational approached (see Dimakopoulos *et al*. 2017)

4. Results and analysis

4.1. Force calculation method for measurement results

The validation explored in this section is presented in three parts. The closed chamber and fully open cases, representing the extremes, are explored in turn, before the results for operating condition are presented. As this is an intentionally conservative model, the contribution from pressures acting seaward on the inside of the front wall are not considered. (These pressures will be small compared to the rear wall pressures, and in any case, would reduce the sliding and over-turning moment of the structure, thus improving the structure stability.) The areas considered for the force acting on the structure are shown by Figure 11.

The model is validated using maximum positive pressures measured for each zero up-crossing wave cycle. Model validation in regular and irregular seas will be done separately but using the same methodology.

Table 1. Regular wave conditions tested.

Name	T (s)	H (m)
Reg01	3	0.26
Reg02	3	0.39
Reg03	3	0.52
Reg04	3	0.65
Reg05	3	0.78
Reg06	4	0.4
Reg07	4	0.6
Reg08	4	0.8
Reg09	4	1
Reg10	4	1.2
Reg11	5	0.67
Reg12	5	0.81
Reg13	5	1.07
Reg15	5	1.61

Reg16	6	0.67
Reg17	6	1
Reg18	6	1.33
Reg19	6	1.67
Reg20	6	0.34
Reg21	3	0.2
Reg22	3	0.15
Reg23	3	0.1
Reg24	4	0.2
Reg25	4	0.15
Reg26	4	0.1
Reg27	6	0.2
Reg28	6	0.15
Reg29	6	0.1

Table 2. Irregular wave conditions tested.

Name	T_p (s)	$H_{m0,i}$ (m)
Irr01	3	0.26
Irr02	3	0.39
Irr03	3	0.52
Irr04	4	0.4
Irr05	4	0.6
Irr06	4	0.8
Irr07	5	0.54
Irr08	5	0.81
Irr10	6	0.67
Irr11	6	1
Irr13	4.5	0.26

The force calculation uses a 2D force per metre run. The experimental force, on the other hand, will be calculated using summed pressures from centred rectangles. This assumes a pressure measurement at each transducer location to be representative of the pressure over an associated area. The scheme is illustrated in Figure 12, with the contributing forces (F_{meas}) for N number of sensors calculated using Equation 19. The rear wall force calculation uses the same method as used for the front wall.

$$F_{meas} = \sum_{n=1}^{N} F_n = \sum_{n=1}^{N} (x_n - x_{n-1}) p_n \qquad (19)$$

There are two ways to quantify forces that might be used in design calculation. The first way is to sum all forces at each time step to give a time history of total forces on the rear wall and

ceiling. The second way takes a worst case approach using the maximum pressure identified for each pressure transducer location (which will not in general be simultaneously experienced). These are then integrated to give the maximum imaginable forces on the rear wall and chamber ceiling.

Here p_n denotes the pressure measured at the location n. For this large scale test, N is equal to 5 and the front wall higher than X_5 is not considered.

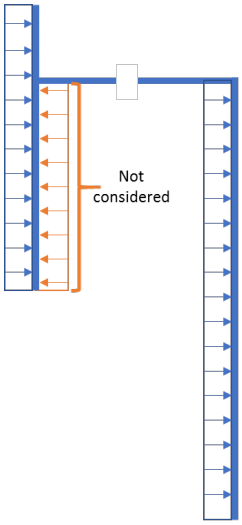

Figure 11 The area considered for the force calculation. The area of the front wall facing the chamber is not considered

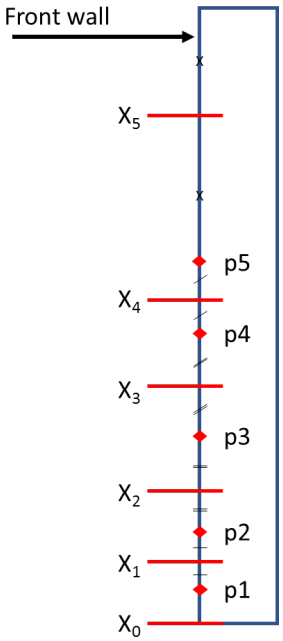

Figure 12 The interval calculation for the rectangular force per metre run method

4.2. Regular wave conditions

4.2.1. Closed chamber

The effectiveness of the model is explored in Figure 13 in which the ratio of measured maxima : predicted calculation, $(p_{c,max})_{\text{measured}}$: $(p_c)_{\text{concept}}$ (solid icons) and $(F_{rear,max})_{measured}$: $(F_{rear})_{concept}$ (hollow icons) for the fully closed chamber is plotted over the range of the wave steepnesses tested. For the chamber pressure maxima comparison ($p_{c,max}$), the averaged between the highest pressure measured by P6 and P7 (located on the chamber ceiling) is taken. For the maxima of the total rear wall force (F_{rear}), pressure transducer P8 to P12 were used with the calculation technique described in Figure 12. Different symbols distinguish different wave periods. The solid line here represents perfect agreement, with points above the line unsafe (under-estimation) and points below the line safe (over-estimation). The agreement is generally very encouraging, with all data lying within a factor of approximately 1.25 of the predictions for both chamber pressure and rear wall force.

Figure 14 (a)-(c) illustrate pressure distributions acting on the rear wall for the model (solid line) and the measurements (solid circles). Here pressures are plotted against the vertical elevation of the corresponding pressure transducer. As expected, Figure 14 (a) and (b) show that the calculated pressures don't differ too much from the measurements because this case assumed that the momentum from the incident wave is transmitted instantaneously to the rear wall and distributed uniformly on the rear wall (Section 3). Figure 14 (c), on the other hand, shows a conservative model prediction for the higher wave steepness sea condition (Reg08). These give confidence in the model for the fully closed condition.

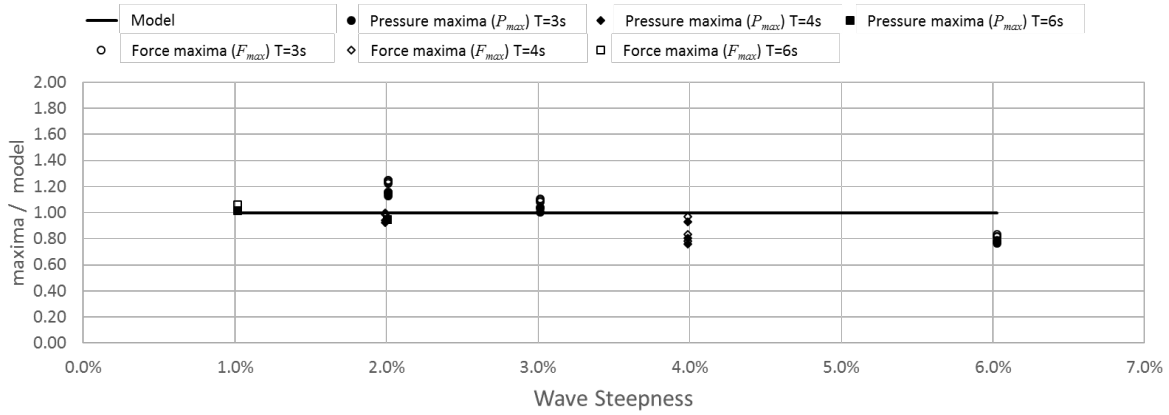

Figure 13 The ratio between measured and predicted chamber pressures (P) and total force (F) for closed chamber case, regular waves.

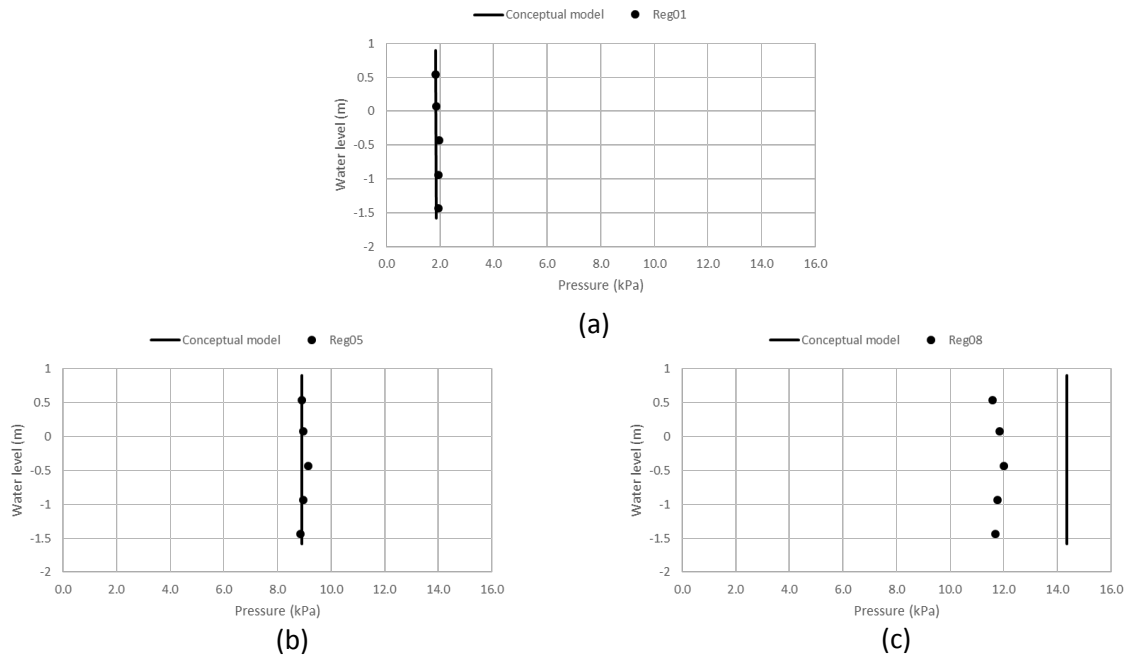

Figure 14 Measured and predicted distributions of pressure maxima, for closed case; regular waves; (a) Reg01, (b) Reg05, and (c) Reg08.

4.2.2. Fully Open chamber condition

For the open chamber case, the chamber pressure remains very close to atmospheric pressure under all conditions tested. The biggest orifice opening in the experiment is 0.3m (1.99%). If the wave length is long enough and the wave height is relatively low, the air inside the chamber will flow freely out of and into the chamber without significantly raising and lowering the chamber pressure. This assumption of no pressure change may not hold for steeper wave conditions, so it is important to differentiate which of the cases may be treated as fully open and which should instead be considered as in "operating condition". The discrimination is done by calculating a measure of the rate of increase of the chamber pressure. This is calculated by dividing the maximum pressure chamber measured by the pressure rise time (from atmospheric pressure to maximum – about ¼ of the wave period). Plotting the pressure rise rates against wave steepness gives Figure 15. As can be seen, every case above a pressure rise rate of 1.5 kPa/s (red line) is considered in the operating condition.

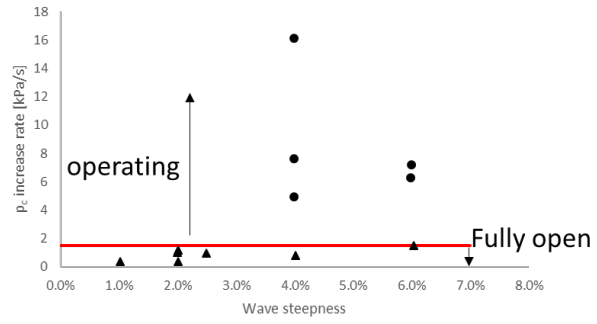

Figure 15 The chamber pressure rise rate for the 2.00% orifice to chamber ratio case, regular waves.

For the conditions identified as 'fully open' the force ratio between the measured and predicted forces are plotted in Figure 16. The model works best for lower wave steepnesses,

with predictions good to within a factor of 1.2. For the steeper wave conditions, the model gives safe prediction by factors ranging from 0.7 to 0.4.

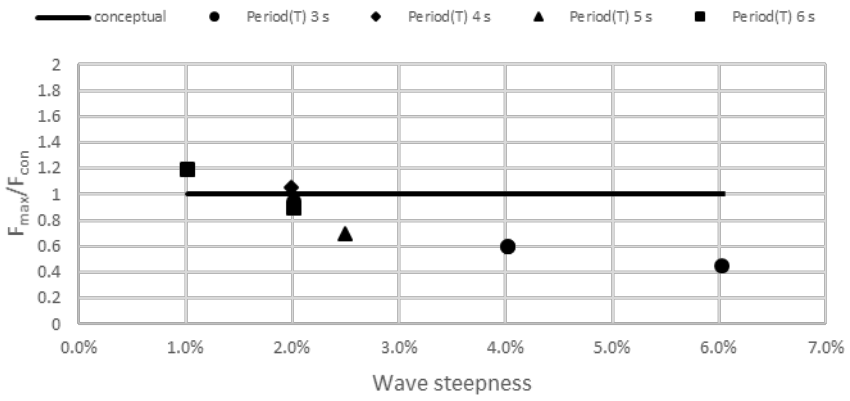

Figure 16 The ratio between the measured and predicted total force acting on the structure, for the fully open case, regular waves.

Maximum measured pressures at each elevation are now compared with pressures predicted by the model in Figure 17. The different data sets show the ratio of measured to predicted pressures for different regular waves (wave steepness shown in the brackets). The solid line represents perfect agreement with the model. The points on the right side of the line are under-estimations (unsafe) and the points on the left side of the line are over-estimations (safe). The measurements mostly fell within a factor of ±0.2 of the model's predictions except for the high wave steepness. It is possible that the higher wave steepnesses are verging on being in the operating condition rather than the fully open condition being explored here.

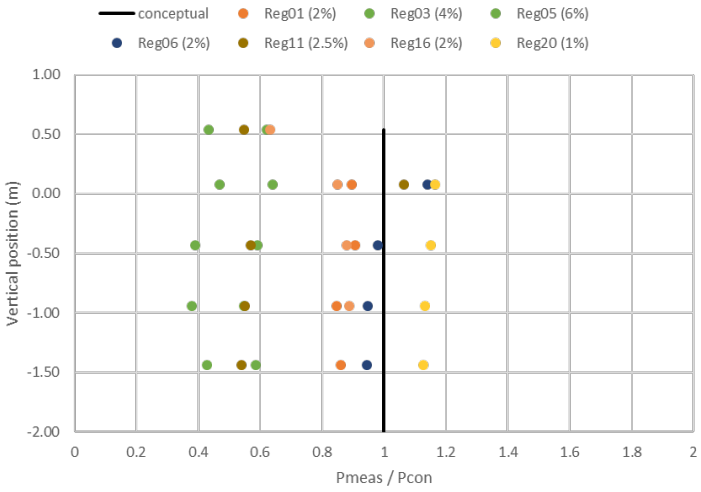

Figure 17 The ratio between measured and predicted chamber pressures, by vertical level, for the fully open case, regular waves.

Figure 18 (a), (b), and (c) show example pressure maxima distributions comparing measured and model prediction on the rear wall with waves Reg01, Reg06, and Reg03 respectively. In the figure, subfigures (a) and (b) show cases where the models are in good agreement with the measurement, whereas (c) shows a safe prediction by a factor of 0.7 in the maximum pressure.

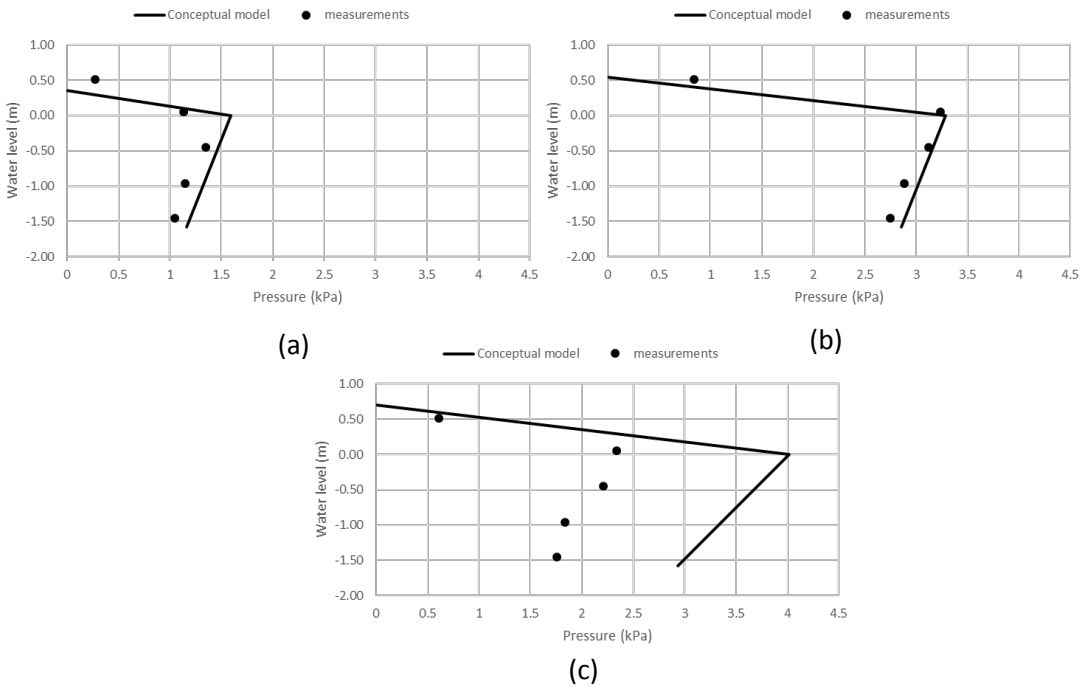

Figure 18 Measured and predicted vertical distributions of pressure maxima, for fully open case; regular waves; (a) Reg01, (b) Reg06, and (c) Reg03.

4.2.3. Operating condition

In the "operating condition", the orifice opening of the caisson chamber was changed, simulating the power take off resistance during operation. The air chamber pressure will mainly be affected by the orifice area relative to the chamber cross-sectional area. For the purpose of simplicity, as a first approximation, it is assumed that only this ratio determines the PTO influence on the chamber pressure. This assumption along with the simplification between the air damping characteristic and the weighting coefficient (P) introduced in Section 2.5, results in an empirically derived Equation 20.

$$P = f\left(\frac{A_o}{A_c}\right) = 1 - 45.55\,(\frac{A_o}{A_c}) \qquad (20)$$

Figure 19, Figure 20, and Figure 21 show the ratio of measured to predicted chamber pressures against the wave steepness, wave height, and wave period respectively. The model validation includes the test results for 0.06%, 0.22%, and 0.88% orifice to chamber area ratio as explained in Section 3, and the 2.00% ratio identified as being in the operating condition as explained in Section 4.1.2. The reliability of the model is more sensitive to wave height than to wave period. From the results, it can be inferred that the prediction is safe for the higher and steeper wave conditions. This may happen because momentum loss during water movement inside the chamber is neglected in the model. It is also notable that higher and steeper wave conditions have a higher likelihood of 'sloshing' occurring within the chamber.

Figure 22 compares example rear wall pressure measurements (solid circles) and predictions (solid line) for a wide range of wave conditions for the 0.88% orifice. Pressures plotted in these figures have the chamber pressure subtracted at each time step leaving only the pressure

induced by the motion of the water. Figure 22 (a), (c), (f), (n), and (o) show a very good agreement between measurement and model. Figure 22 (b), (e), (g), (h), and (m) show rather less good agreement, but still to within a factor of 0.6 (a safe prediction). Figure 22 (j) and (k) show an interesting feature where the pressures change dramatically over the vertical water level. The maximum pressure acting near the still water level is however similar with the model, to factor of 0.72 to 0.76. This unusual pattern may happen because momentum is dissipated by the water surface sloshing during the experiment. The simple model assumes the water surface to be well behaved, like a piston. Figure 22 (d) and (l) show the model giving quite significant over-estimations (a factor of 0.3 to 0.4 between model and measurements). Nevertheless, almost all of the data show a safe prediction.

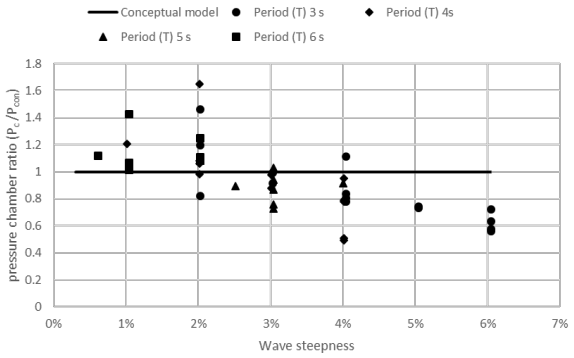

Figure 19 The ratio between measured and predicted chamber pressures against the wave steepness in the operating condition, regular waves.

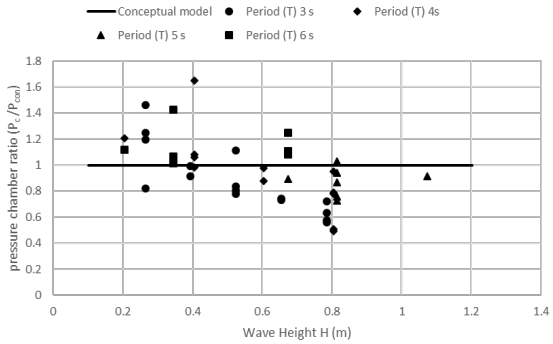

Figure 20 The ratio between measured and predicted chamber pressures against the wave height in the operating condition, regular waves.

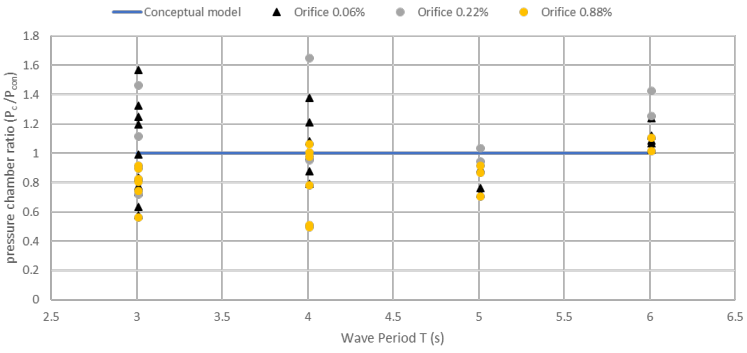

Figure 21 The ratio between measured and predicted chamber pressures against the wave period in the operating condition, regular waves.

4.2.4. Vertical force on the chamber ceiling

An OWC breakwater has a pressure acting on the chamber ceiling. These pressures act to lower the net weight, reducing friction against sliding, and contributes to overturning moments for the complete structure. It is therefore important to estimate the ceiling vertical force. Only the positive (upward) force acting on the ceiling will be considered for this estimation because the negative force will always result in the structure being safer against sliding and overturning. The success of the model is evaluated in Figure 23 where the ratio of measured to predicted vertical force is plotted over the range of wave heights, for the closed chamber condition. The model accurately predicts vertical forces to within a factor of 1 ± 0.2.

Since the maximum chamber pressure will be experienced in the closed chamber case, only this case is plotted. The ratio of measured vertical forces in closed and operating conditions in Figure 24 supports this assertion. The fully open condition is not included in this figure because it is assumed to have zero chamber pressure. As predicted, the ratio decreases as the orifice opening gets bigger. Note that some of the 0.06% orifice cases are located above the line of perfect agreement. This may be because the orifice to chamber area ratio is very small (0.06%) making the difference between the closed chamber and the operating condition negligible, especially for the larger wave height conditions.

When compared to the total horizontal force, the vertical force for the regular wave conditions is always less by a factor of approximately 0.8. This result is in line with the suggestion of previous research (Ashlin *et al.,* 2017).

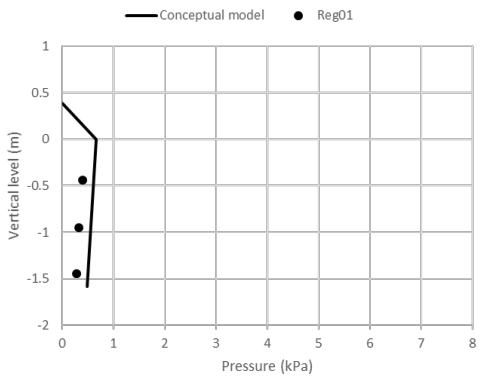
Conceptual model
Reg01
Vertical level (m)
Pressure (kPa)

(a)

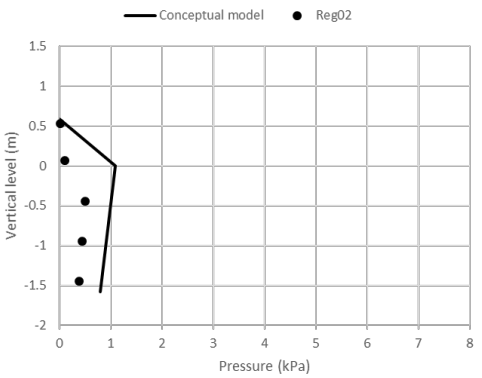
Conceptual model
Reg02
Vertical level (m)
Pressure (kPa)

(b)

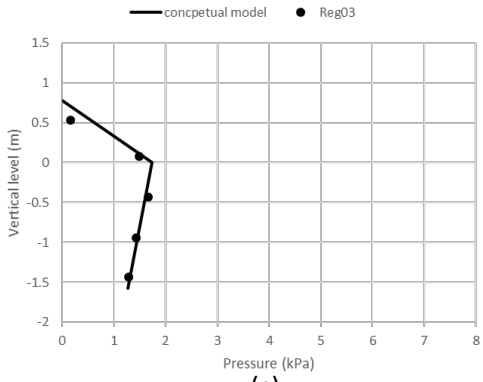
concpetual model
Reg03
Vertical level (m)
Pressure (kPa)

(c)

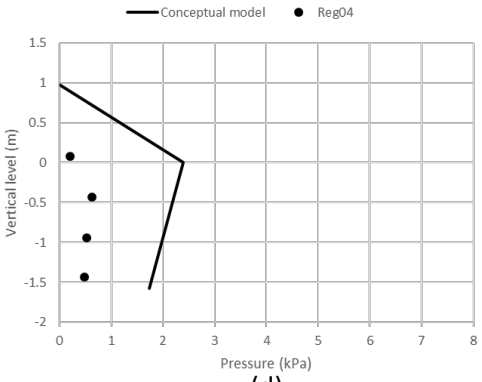
Conceptual model
Reg04
Vertical level (m)
Pressure (kPa)

(d)

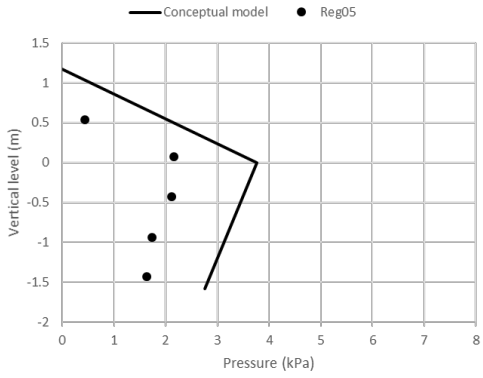
Conceptual model
Reg05
Vertical level (m)
Pressure (kPa)

(e)

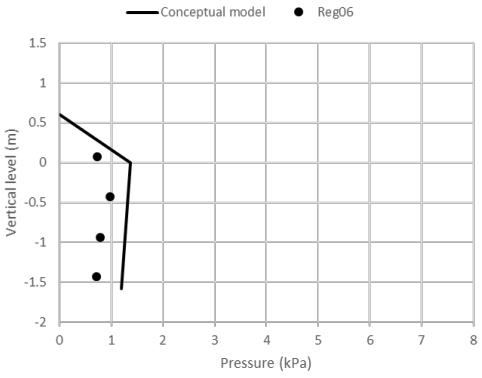
Conceptual model
Reg06
Vertical level (m)
Pressure (kPa)

(f)

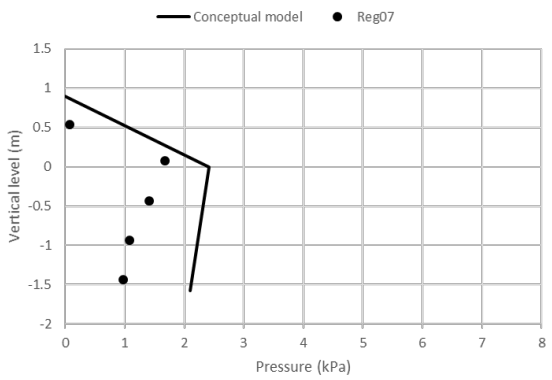
Conceptual model
Reg07
Vertical level (m)
Pressure (kPa)

(g)

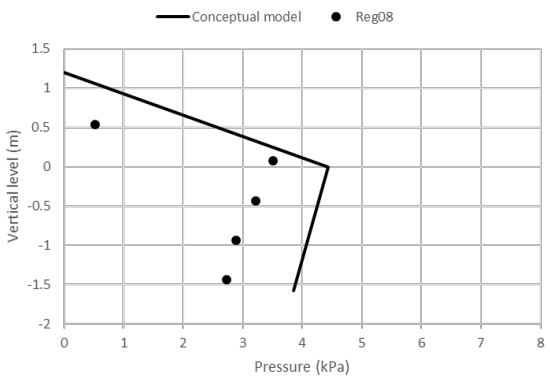
Conceptual model
Reg08
Vertical level (m)
Pressure (kPa)

(h)

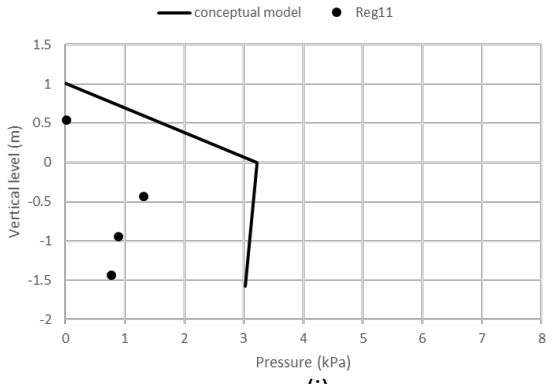
conceptual model
Reg11
Vertical level (m)
Pressure (kPa)

(i)

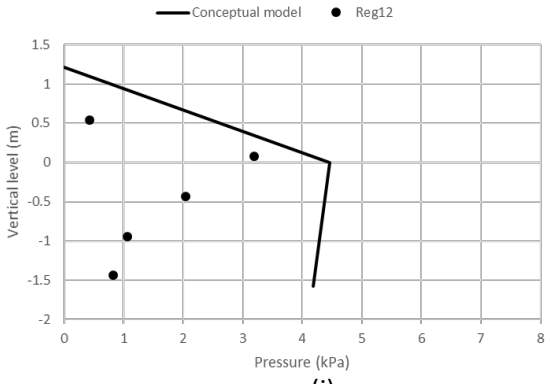
Conceptual model
Reg12
Vertical level (m)
Pressure (kPa)

(j)

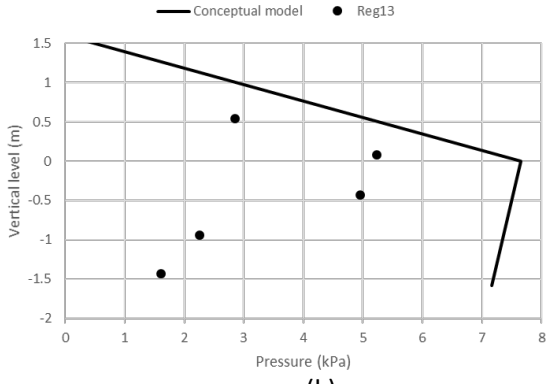
Conceptual model
Reg13
Vertical level (m)
Pressure (kPa)

(k)

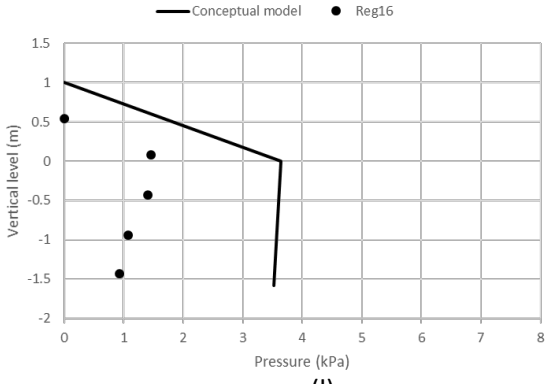
Conceptual model
Reg16
Vertical level (m)
Pressure (kPa)

(l)

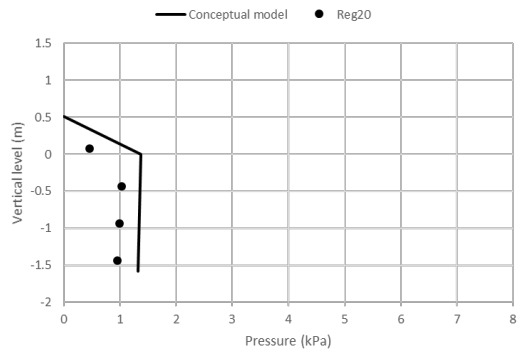

(m)

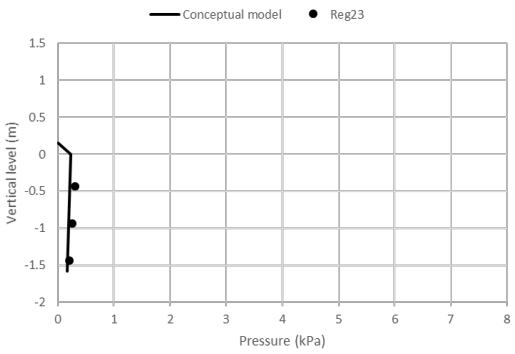

(n)

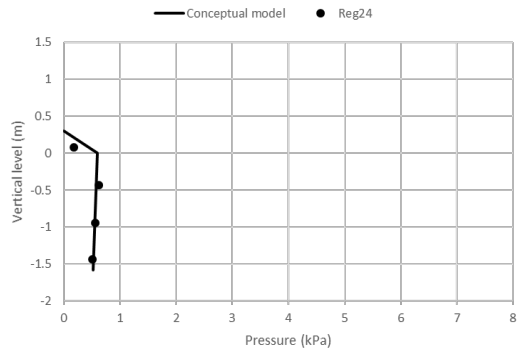

(o)

Figure 22 (a) – (o) The pressure distribution acting on the rear wall at various pressure transducer vertical elevation for different wave settings

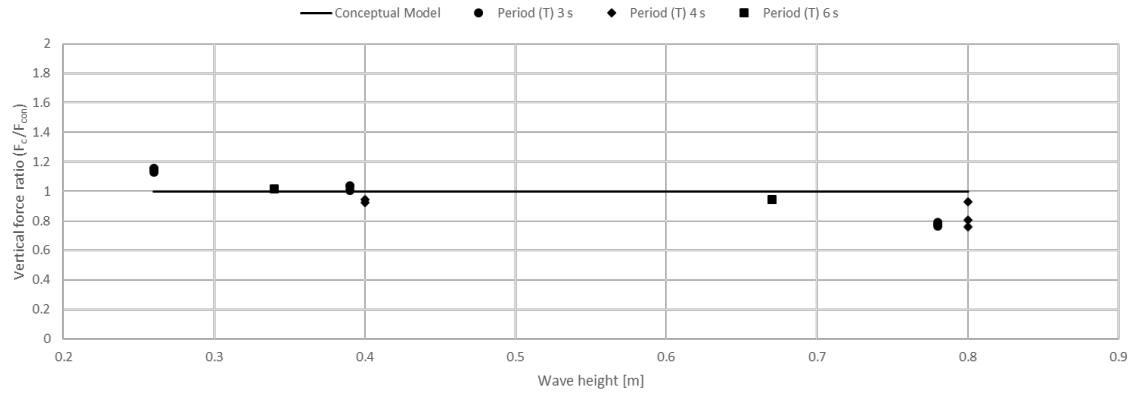

Figure 23 Ratio between the measured and predicted vertical forces against the wave height for closed chamber case, regular waves.

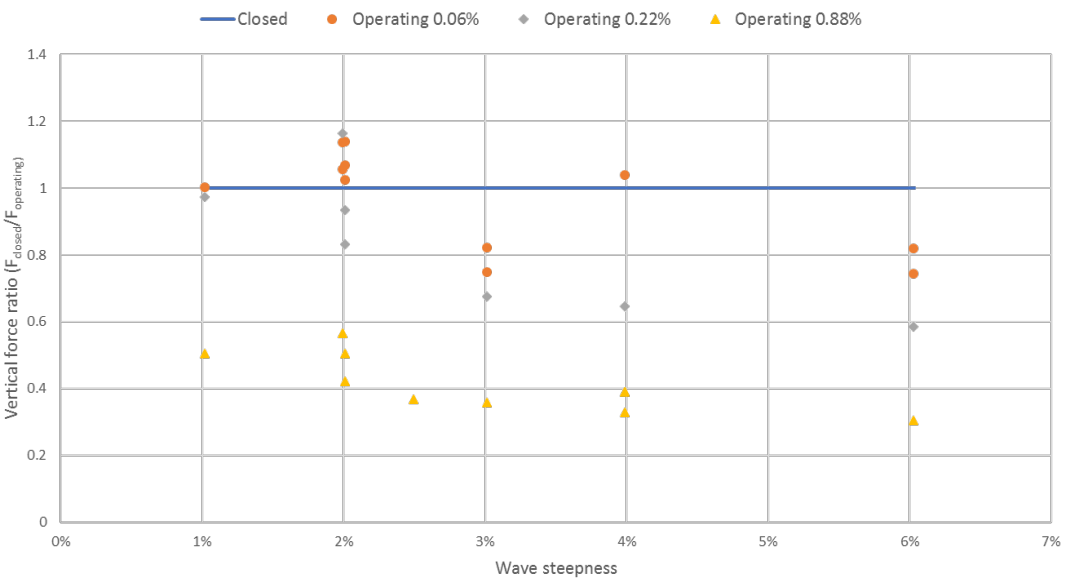

Figure 24 Caisson chamber vertical forces; ratio between the 'closed' and 'operating' conditions, for regular waves

4.3. Irregular wave conditions

To explore whether the new prediction method could be applied to irregular wave conditions, it was assumed that individual wave heights were Rayleigh-distributed, in which case the H_{max} will be approximately 1.8 times H_s for a sequence of 1000 waves. Recalling that the model attempts to predict worst case loadings, a simple approach to adjusting the model is therefore to multiply the wave height by this factor of 1.8. This change will affect the force on the front wall (F_{Goda}) in Equation 3. Due to the required test lengths, rather fewer irregular wave experiments were carried out so the validation data set is sparser than for regular waves. As previously, the following sections explore the closed, open and operating regimes in turn (in sections 4.3.1; 4.3.2 and 4.3.3 respectively).

4.3.1. Irregular wave conditions, closed chamber

The ratio between the maximum measured to predicted chamber pressure is presented in Figure 25 in the usual way.

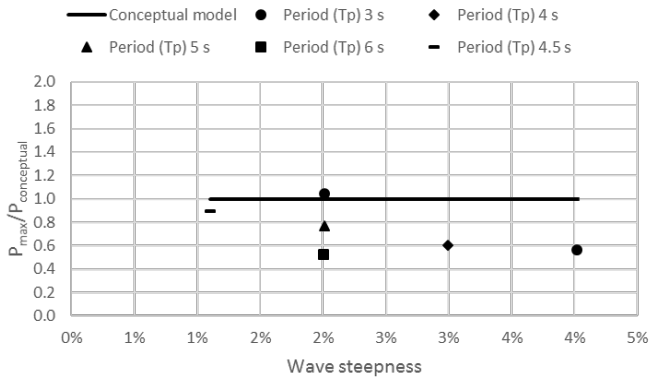

Figure 25 The ratio between measured and predicted chamber pressures for closed chamber case, irregular waves.

The model fits well with the measurements especially for the lower wave steepness, where the measured / predicted ratio is 1 ± 0.1. For higher waves, the prediction factor is about 0.6 to 0.8, all falling in the safe zone.

4.3.2. Irregular waves conditions, open chamber

First, it is necessary to distinguish with care the tests which are truly 'open condition' from those still effectively 'operating conditions'. The method used to distinguish these cases for regular waves – discriminating on the chamber pressure increase rate – cannot be applied straightforwardly here. If the maximum pressure is considered, then most of the tests would be defined to be 'operating condition'. Instead, the average of the pressure increase rates associated with the four largest pressure maxima events for each test is used as the basis for the pressure increase rate cut-off, analogous to Goda's use of $F_{1/250}$. Figure 26 shows the ratio of the measured rear wall force and the force predicted by the model for the cases which the averaged increase rate suggests fully open conditions (< 1.5 kPa/s).

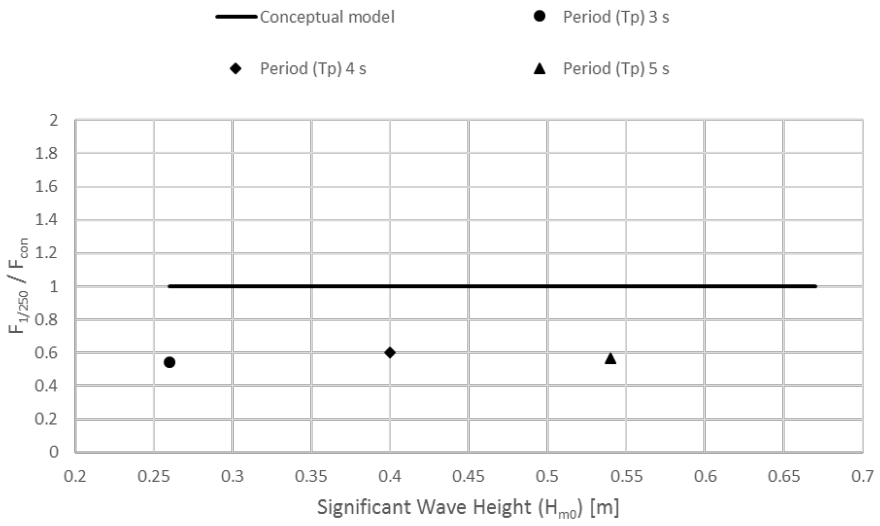

Figure 26 The ratio between the measured and predicted total force acting on the structure, for the fully open case, irregular waves.

The x-axis shows H_s because all of these data have the wave steepness ≈ 2%. The model generally over-predicts the measurements, with the comparison factor of about 0.6. Since the maximum pressure acting on the rear wall may depend upon the elevation, Figure 27 (a) – (c) show comparisons between model (solid black line) and predicted (non-simultaneous) maximum measured pressure distributions, with the irregular wave cases Irr01, Irr04 and Irr07.

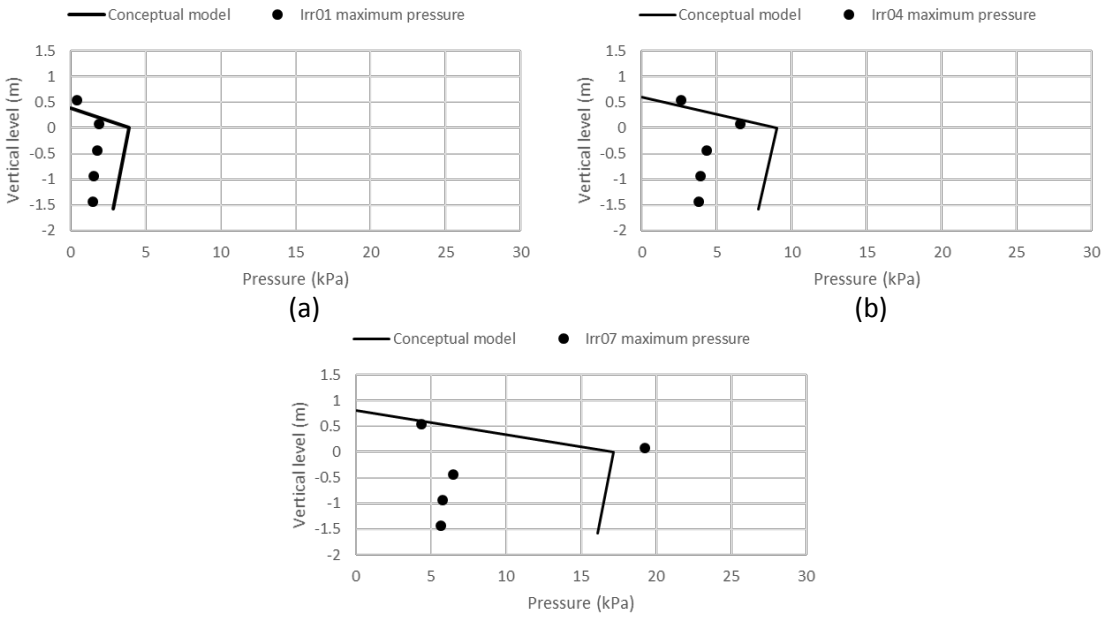

Figure 27 Rear wall pressure distributions, measurement and the model prediction, for fully open case for; (a) Irr01, (b) Irr04, and (c) Irr07.

As can be observed from Figure 27, the measured pressure maxima are safely predicted. For Irr07 where the water level pressure is significantly higher, these pressures might be due to sloshing in the chamber. Compared to data shown in Figure 26, however, the force prediction for this case is still safe. This effect is evidenced in detail in Figure 28 which shows the associated 'sloshing' (a) the instant of the pressure maximum, and (b) immediately afterwards. It is clear that the in-chamber behaviour is far from an idealised up and down oscillation, but instead, the water located near the rear wall is observed to run up the rear wall very rapidly, before hitting the ceiling. This water is then reflected to the front part of the chamber.

Figure 28 In-chamber view (a) at the instant of violent sloshing and (b)immediately after. Irregular waves (Irr07)

The water surface movement can be compared with the well-behaved oscillation taken from Irr01 test shown in Figure 29.

(a) (b)

Figure 29 In chamber view of (a) the negative and (b) the positive water movement of Irr01 irregular wave settings, the still water level is located at 0.73 m on the in-chamber markers.

4.3.3. Irregular waves conditions, operating condition

For 'operating' conditions, Figure 30 shows the ratio of maximum measured chamber pressure to that predicted, plotted against the wave steepness. For these 'operating conditions' under irregular waves, the model predictions are again safe, within a factor of 0.6 ± 0.2.

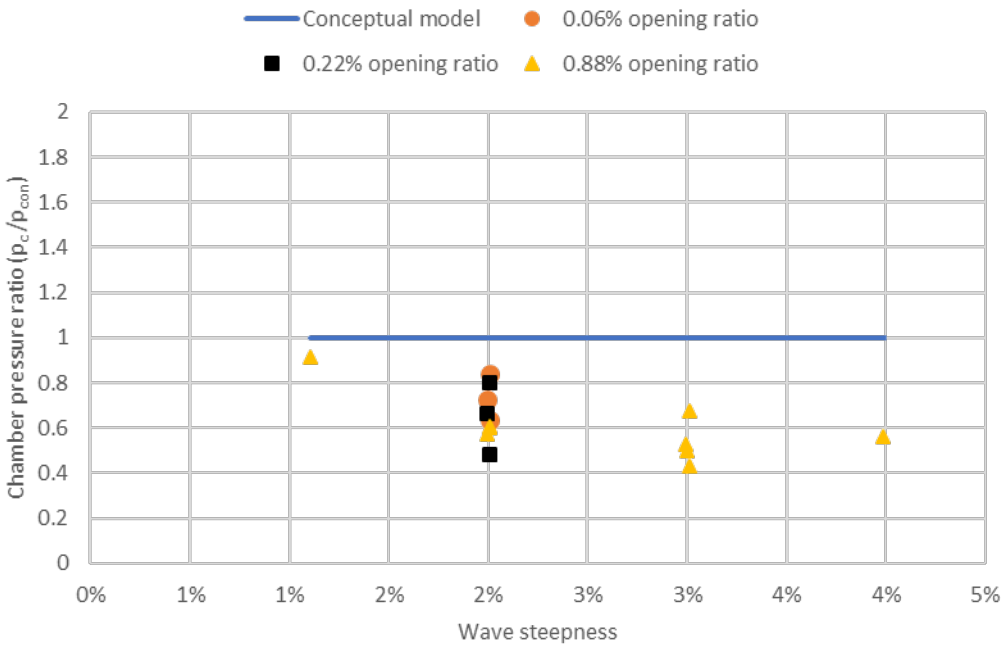

Figure 30 Ratio of measured to predicted maximum chamber pressure; operating conditions; irregular waves.

5. Discussion of physical basis of model

During the experiment, it can be observed that the water level inside the caisson is not always well behaved. For example, there were instances where the water near to rear wall rose up and hit the ceiling at the same time as the water level near the front wall fell to near the 'lip' opening. This motion then reversed to hit the ceiling at the front wall while water at the rear wall fell below still water level. This situation is quite different from our simple model upon

which the prediction method is based as wave momentum is no longer being transmitted as in the model. This water movement is called ‘sloshing’ and Figure 31 (a) and (b) show images of ‘sloshing’ during one of the experiments.

(a) (b)

Figure 31 In chamber view of the caisson (a) just before and (b) during sloshing which occurred in the Reg13 wave condition experiment.

In addition to the sloshing, some of the wave condition could also lead to ‘venting’ which suspected to occur in Figure 32 during the Reg15 experiment. This condition occurs when the water level inside the caisson falls below the ‘lip’ of the front wall. This condition allows the pressure inside the caisson to equalise with the atmospheric pressure through the ‘lip’ opening. Although it might affect the performance of the OWC, it has little influence for the pressure experienced on the rear wall. A red line in Figure 32 gives an estimation of the front ‘lip’ location and as can be seen from the figure, the water surface fell below the line.

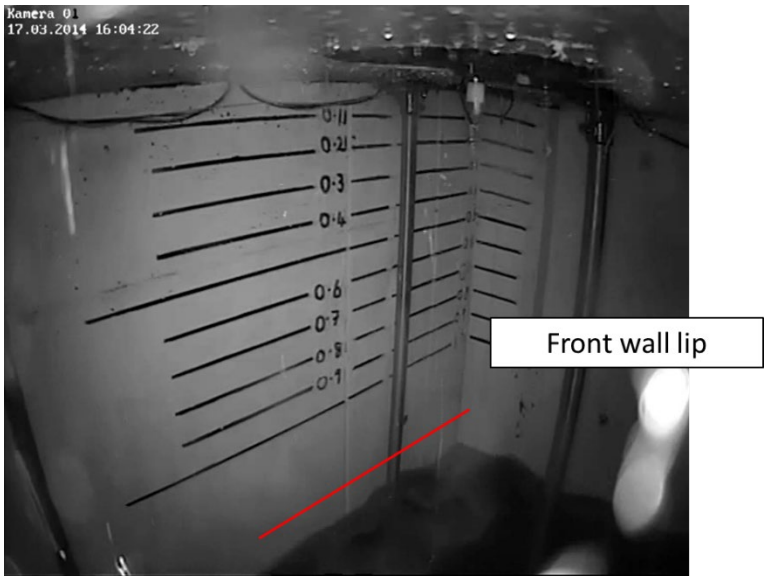

Figure 32 Inside view of ‘venting’ during the Reg15 experiments.

6. Conclusion

A new model for the prediction of wave loads experienced by an OWC caisson has been presented. This is based upon consideration of the physical processes at work, and where possible draws upon established models for conventional caisson breakwaters. The load model considers three OWC chamber regimes: closed chamber, fully open condition, and operating condition. Both regular and irregular waves were tested.

Data from a campaign of large-scale experiments carried out at the Large Wave Flume (GWK) in Hannover, Germany (Viviano *et al*., 2016) has been used to validate the model. The measurements were carried out with five different circular orifice setting diameters of: 0 m, 0.05 m (0.06%), 0.1 m (0.22%), 0.2 m (0.88%), and 0.3 m (1.99%). The different orifice settings are aims to represent the varying power-take-of damping characteristics during operation.

The model has been tested against multiple chamber conditions in regular waves. The closed chamber model agreed very well with the proposed model, to a factor of 1±0.2 for all of the cases for both the chamber pressure measurement and the rear wall force calculation. For the fully open condition, the rear wall measurement:prediction shows somewhat greater spread across the range of wave steepnesses. The model works better for the lower wave steepnesses (within a factor of 1.2) while the model over-predicted the forces for the higher wave steepnesses with an agreement factor between 0.4 to 0.7, *i.e.* a conservative prediction. The chamber pressure measured:prediction comparison shows that the model is safer for the higher wave height and under-predicts for the lower wave height. The model works well for the wave steepness of 3% with an agreement factor of 0.9 ± 0.2. The vertical force measured:prediction calculation shows that the structure experience highest vertical force during the closed chamber condition under well behaved water column situation, and the model able to predict the measured vertical force for the closed chamber to within a factor of 1 ± 0.2.

When the structure is exposed to irregular waves, the model slightly over-predicts the pressure measurements and inferred forces to within a factor between 0.6 to 0.8 for the closed chamber, fully open chamber, and operating conditions. These results indicate a conservative (safe) model.

The delivered model is thus a design tool to predict the pressure distributions, total maximum horizontal forces, and caisson chamber vertical forces under non-breaking wave conditions. These parameter predictions can be incorporated into calculations for the over-turning moment and safety against sliding for the whole structure.

Acknowledgments

For the original GWK tests, the authors are grateful to University of Edinburgh, HR Wallingford, University of Campania "Luigi Vanvitelli", Queen's University Belfast, and University of East Anglia for supporting staff time devoted for this project and to Drs. John Alderson (HR Wallingford), Viviana Russo (Queen's University of Belfast), Vincenzo Ferrante (Second University of Naples), Matthias Kudella (GWK) and the support team at the GWK for design, construction, and testing of these experiments. The Authors also thank Antonino Viviano (University of Catania) and Stefania Naty (University of Catania) for the helpful analysis published in Viviano *et al*. (2016). Important input to the design of the GWK experiments from Professor Trevor Whittaker (Queen's University Belfast) and Dr Mark

Cooker (University of East Anglia). The access to the GWK facility provided by the European Community's Seventh Framework Progamme through the Integrating Activity HYDRALAB IV, Contract no 261520. The authors also acknowledge the help of Nic Miller and David Bourke (University of Edinburgh), Mariangela Sfouni-Grigoriadou, Encarnacion Median-Lopez, Giovanni Cuomo, and Daniele Longo (HR Wallingford) for follow up discussions after the GWK tests. Krisna Pawitan would like to express his gratitude to Indonesia Endowment Fund for Education (LPDP) for the financial support for his studies in Edinburgh.

References

Allsop, W., Bruce, T., Alderson, J., Ferrante, V., Russo, V., Vicinanza, D. & Kudella, M., 2014. Large scale test on a generalised oscillating water column wave energy converter. *Proc. HYDRALAB IV Joint User Meeting*, Lisbon.

Arena, F., Romolo, A., Malara, G. & Ascanelli, A., 2013. On design and building of a U-OWC wave energy converter in the Mediterranean Sea: a case study. Proc. *32nd Int. Conf. on Ocean, Offshore, and Arctic Engineering ("OMAE 2013")* Nantes, France.

Ashlin, S.J., Sundar, V. and Sannasiraj, S.A., 2017. Pressures and Forces on an Oscillating Water Column–Type Wave Energy Caisson Breakwater. *Journal of Waterway, Port, Coastal, and Ocean Engineering*, *143*(5), p.04017020-1 - 18.

Azzellino, A., Contestabile, P., Ferrante, V., Lanfredi, C., Vicinanza, D. (2011). "Strategic Environmental Assessment to evaluate WEC projects in the perspective of the environmental cost-benefit analysis", Proceedings of the 21th International Conference ISOPE, Maui, Hawaii, USA, ISBN 1–880653-60–5, pg.709-715.

Boake, C. B., Whittaker, T. J. T., Folley, M. & Ellen, H., 2002. Overview and initial operational experience of the LIMPET wave energy plant., *Proc. 12th Int. Offshore & Polar Eng. Conf. ("ISOPE 2002")*, pp. 586-594.

Boccotti, P., 2003. On a new energy absorber. *Ocean Eng.,* 30, pp. 1191-1200 (Elsevier).

Buccino, M., Banfi. D., Vicinanza, D., Calabrese, M., Giudice, G. D. & Carravetta, A., 2012. Non breaking wave forces at the front face of seawave slotcone generators. *Energies,* 5, pp. 4779-4803 (Elsevier).Buccino, M., Dentale, F., Salerno, D., Contestabile, P., Calabrese, M. (2016). "The use of CFD in the analysis of wave loadings acting on seawave slot-cone generators" . Sustainability (Switzerland) 8(12),1255

Buccino, M., Dentale, F., Salerno, D., Contestabile, P., Calabrese, M. (2016). "The use of CFD in the analysis of wave loadings acting on seawave slot-cone generators" . Sustainability (Switzerland) 8(12),1255

Buccino, M., Stagonas, D. & Vicinanza, D., 2015a. Development of composite sea wall wave energy converter system. *Renewable Energy,* 81, pp. 509-522 (Elsevier).

Buccino, M., Vicinanza, D., Salerno, D., Banfi, D. & Calabrese, M., 2015b. Nature and magnitude of wave loadings at seawave slot-cone generators. *Ocean Eng.,* 95, pp. 34-58 (Elsevier).

Contestabile, P., Iuppa, C., Di Lauro, E., Cavallaro, L., Lykke Andersen, T., Vicinanza, D. (2017). "Wave loadings acting on innovative rubble mound breakwater for overtopping wave energy conversion",

Coastal Engineering, ISSN 0378-3839, vol. 122, pp. 60–74.
http://dx.doi.org/10.1016/j.coastaleng.2017.02.001

Dimakopoulos, A., Cooker, M. & Bruce, T., 2017. The influence od scale on the air flow and pressure in the modelling of Oscillating Water Column Wave Energy Converter. *Int. J. Marine Energy,* 19, pp. 272-291 (Elsevier).

Falcão, A. F. O. & Henriques, J. C. C., 2015. Oscillating-Water-Column wave energy converters and air turbines: A review. *Renewable Energy,* Volume 85, pp. 1391-1424 (Elsevier).

Faraci, C., Scandura, P. & Foti, E., 2015. Reflection of Sea Waves by Combined Caissons. *J. Waterway, Port, Coastal and Ocean Eng., Volume 141, p. 04014036*

Folley, M., Whittaker, T. & Osterried, M., 2004. The Oscillating Wave Surge Converter. *Proc. 14th Int. Conf. Ocean and Polar Eng. ("ISOPE")*, Toulon, pp. 189-193.

Goda, Y., 2000. *Random Seas and Design of Maritime Structures, Advanced Series on Ocean Engineering.* World Scientific, Singapore.

Iuppa, C., Contestabile, P., Cavallaro, L., Foti, E., Vicinanza, D. (2016). "Hydraulic performance of an innovative breakwater for overtopping wave energy conversion", Sustainability, ISSN 2071-1050, 8(12), 1226; http://dx.doi.org/10.3390/su8121226

Kriebel, D. L. & Bollman, C. A., 1996. Wave transmission past vertical wave barriers. *Proc. 25th Int. Conf. Coastal Eng.*, pp. 2470-2483 (ASCE).

Kuo, Y.-S., Lin, C.-S., Chung, C.-Y. & Wang, Y.-K., 2015. Wave loading distribution of oscillating water column caisson breakwaters under non-breaking wave forces. *J. of Marine Sci, and Techn.,* 23(1), pp. 78-87 (Springer).

Medina-Lopez, E., Allsop, W., Dimakopoulos, A. & Bruce, T., 2015. Conjectures on the failure of the OWC breakwater at Mutriku., *Proc. Coastal Structures '15*., Boston (ASCE).

Moretti, G., Rosati, G., Alves, M., Grases, M., Vertechy, R., and Fontana, M., 2015. Analysis and design of an oscillating water column wave energy converter with dielectric elastomer power take-off*. Proc. 34th Int. Conf. Ocean, Offshore and Arctic Eng. ("OMAE 2015")*, Newfoundland, Canada (ASME).

Morris-Thomas, M. T., Irvin, R. J. & Thiagarajan, K. P., 2007. An investigation into the hydrodynamic efficiency of an oscillating water column. *J. Offshore Mechanics and Arctic Eng.,* 129, pp. 273-278 (ASME).

Neumann, F. & Crom, I. L., 2011. Pico OWC - the Frog Prince of Wave Energy? Recent autonomous operational experience and plans for an open real-sea test center in semi-controlled environment*. Proc. 9th European Wave and Tidal Energy Conf ("EWTEC 2011")*, Southampton, UK.

Patterson, C., Dunsire, R. and Hillier, S., 2010. Development of wave energy breakwater at Siadar, Isle of Lewis. In Coasts, marine structures and breakwaters: Adapting to change: Proceedings of the 9th international conference organised by the Institution of Civil Engineers and held in Edinburgh on 16 to 18 September 2009 (pp. 1-738). Thomas Telford Ltd.

Pawitan, K. A. & Bruce, T., 2016. Influence of power take off on front face loads on a small-scale OWC model*. Proc. Asian Wave and Tidal Energy Conf. ("AWTEC 2016")*, pp.486-493.

Raju, V. & Neelamani, S., 1992. Concrete caisson for a 150 kW wave energy pilot plant: design, construction, and installation aspects. *Proc. 2nd Int. Offshore and Polar Eng. Conf. ("ISOPE 1992")*, pp. 584-591.

Retzler, C., 2006. Measurements of the slow drift dynamics of a model Pelamis wave energy converter. *Renewable Energy,* 31, pp. 257-269 (Elsevier).

Takahashi, S., 1988. Hydrodynamic characteristics of wave-power-extracting caisson breakwater. *Proc. 21st Int. Conf. Coastal Eng. ("ICCE '98")*, pp.2489-2503. (ASCE)

Takahashi, S., Nakada, H., Ohneda, H. & Shikamori, M., 1992. Wave power conversion by a prototype wave power extracting caisson in sakata port. *Proc. 23rd Int. Conf. Coastal Eng.*, pp. 3440-3453 (ASCE).

Torre-Enciso, Y., Marqus, J. & de Aguileta, L. L., 2010. Mutriku, Lessons Learnt., *Proc. 3rd Int. Conf. Ocean Energy*, Bilbao.

Vicinanza, D., Contestabile, P., Nørgaard, J. H. & Andersen, T. L., 2014. Innovative rubble mound breakwaters for overtopping wave energy conversion. *Coastal Engineering,* 88, pp. 154-170 (Elsevier).

Vicinanza, D., Dentale, F., Salerno, D., Buccino, M. (2015). "Structural response of seawave Slot-Cone Generator (SSG) from Random Wave CFD simulations". Proceedings of the International Offshore and Polar Engineering Conference. pp. 985-991.

Vicinanza, D., Nørgaard, J. H., Contestabile, P. & Andersen, T. L., 2013. Wave loadings acting on overtopping breakwater for energy conversion. *J. Coastal Research,* 65, pp. 1669-1674 .

Viviano, A., Naty, S., Foti, E., Bruce, T., Allsop, W. & Vicinanza, D., 2016. Large-scale experiments on the behaviour of generalised Oscillating Water Column under random waves. *Renewable Energy,* 99, pp. 875-887 (Elsevier).

Weber, J., 2007. Representation of non-linear aero-thermodynamic effects during small scale physical modelling of OWC-WECs., *Proc. 7th European Wave and Tidal Energy Conf* (Bilbao), pp. 11-14).